This is an open access article published under an ACS AuthorChoice License, which permits copying and redistribution of the article or any adaptations for non-commercial purposes.

ACS APPLIED MATERIALS & INTERFACES

Research Article

Cite This: ACS Appl. Mater. Interfaces 2018, 10, 11152−11163

www.acsami.org

Downloaded via Christian Kuttner on March 13, 2019 at 06:19:07 (UTC).
See https://pubs.acs.org/sharingguidelines for options on how to legitimately share published articles.

# Seeded Growth Synthesis of Gold Nanotriangles: Size Control, SAXS Analysis, and SERS Performance

Christian Kuttner,[†,‡,∇] Martin Mayer,[†,‡] Martin Dulle,[∥] Ana Moscoso,[§] Juan Manuel López-Romero,[§] Stephan Förster,[∥] Andreas Fery,*[,†,‡,⊥] Jorge Pérez-Juste,[#] and Rafael Contreras-Cáceres*[,†,§]

[†]Leibniz-Institut für Polymerforschung Dresden e.V., Hohe Str. 6, 01069 Dresden, Germany

[‡]Cluster of Excellence Centre for Advancing Electronics Dresden (cfaed), Technische Universität Dresden, 01062 Dresden, Germany

[§]Departamento de Química Orgánica, Facultad de Ciencias, Universidad de Málaga, 29071 Málaga, Spain

[∥]Jülich Centre for Neutron Science (JCNS-1) and Institute for Complex Systems (ICS-1), Forschungszentrum Jülich GmbH, 52425 Jülich, Germany

[⊥]Physical Chemistry of Polymeric Materials, Technische Universität Dresden, 01069 Dresden, Germany

[#]Departamento de Química Física, CINBIO, Universidade de Vigo and IBIV, 36310 Vigo, Spain

*Supporting Information*

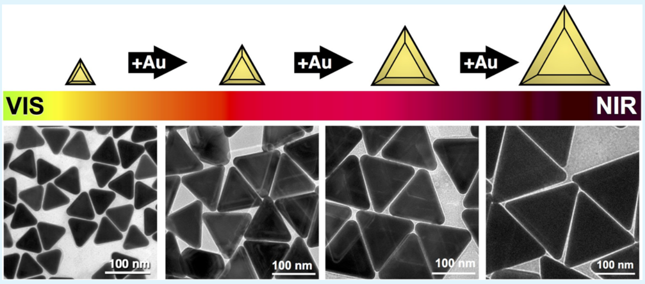

**ABSTRACT:** We studied the controlled growth of triangular prismatic Au nanoparticles with different beveled sides for surface-enhanced Raman spectroscopy (SERS) applications. First, in a seedless synthesis using 3-butenoic acid (3BA) and benzyldimethylammonium chloride (BDAC), gold nanotriangles (AuNTs) were synthesized in a mixture with gold nanooctahedra (AuNOCs) and separated by depletion-induced flocculation. Here, the influence of temperature, pH, and reducing agent on the reaction kinetics was initially investigated by UV−vis and correlated to the size and yield of AuNT seeds. In a second step, the AuNT size was increased by seed-mediated overgrowth with Au. We show for the first time that preformed 3BA-synthesized AuNT seeds can be overgrown up to a final edge length of 175 nm and a thickness of 80 nm while maintaining their triangular shape and tip sharpness. The NT morphology, including edge length, thickness, and tip rounding, was precisely characterized in dispersion by small-angle X-ray scattering and in dry state by transmission electron microscopy and field-emission scanning electron microscopy. For sensor purposes, we studied the size-dependent SERS performance of AuNTs yielding analytical enhancement factors between $0.9 \times 10^4$ and $5.6 \times 10^4$ and nanomolar limit of detection ($10^{-8}$−$10^{-9}$ M) for 4-mercaptobenzoic acid and BDAC. These results confirm that the 3BA approach allows the fabrication of AuNTs in a whole range of sizes maintaining the NT morphology. This enables tailoring of localized surface plasmon resonances between 590 and 740 nm, even in the near-infrared window of a biological tissue, for use as colloidal SERS sensing agents or for optoelectronic applications.

**KEYWORDS:** *gold nanotriangles, seed-mediated approach, plasmonic platforms, ultrasensitive detection, small-angle X-ray scattering, surface-enhanced Raman scattering, colloidal particles*

## INTRODUCTION

Over the past decades, metal nanoparticles (NPs) have been extensively used in many areas of science such as biotechnology,[1,2] targeted drug delivery,[3,4] cancer diagnosis,[5] as well as for sensing and catalytic applications.[6,7] The most important characteristic of noble metal NPs at this range of sizes is their intrinsic optical properties, that is, their localized surface plasmon resonances (LSPRs).[8,9] This feature is based on the collective oscillation of free electrons within the NPs upon interaction with an external electromagnetic source. For noble metals such as Au, Ag, or Cu, this delocalization results in intense extinction bands normally located in the UV−vis−near-infrared (NIR) spectrum, as initially described by Mie theory. Interestingly, the position and the intensity of the LSPR depend on several characteristic factors such as material composition,[9] particle size and shape,[10] and the dielectric environment.[11] Particularly, a tight control over the NP morphology allows the fine tuning of the LSPR position over a wide range of the electromagnetic spectrum.[9] The great success in the synthesis of anisotropic metal NPs with a tight control relies on high confinement of the electromagnetic field at well-defined sharp angles, cavities, or sharp tips, thus leading to further promising and attractive applications in surface-enhanced Raman spectroscopy (SERS).[12−14] Importantly, for

**Received:** December 18, 2017
**Accepted:** March 2, 2018
**Published:** March 2, 2018

ACS Publications © 2018 American Chemical Society

DOI: 10.1021/acsami.7b19081

the efficient use of NPs as colloidal SERS sensors, their optical properties should be matched to a wide range of laser excitation wavelengths. In particular, for bioapplication purposes, the use of low-energy near-infrared lasers is necessary to suppress the fluorescence and utilize the transparency NIR windows of biological samples (650−900 and 1000−1350 nm).[15−17] For this purpose, it would be beneficial to extend the plasmon absorption toward the near-infrared regime, which can be accomplished by increasing the size of NPs.[18] Other recently reported applications for nonspherical metal NPs are hyperthermia for local heating[19] and drug delivery, biological imaging,[20] and the use as building blocks for bottom-up assembly of optical functional materials, wave guides, antenna structures, and optoelectronic circuits.[21,22]

Typically, noble metal NPs are synthesized by wet-chemical processes through the reduction of a precursor salt (e.g., $HAuCl_4$) with a suitable reducing agent in the presence of stabilizing "capping" molecules, which play an important role in controlling the NP morphology.[23,24] Other synthesis parameters such as temperature,[25] pH,[26,27] solvent nature,[28] and presence of ions[29−31] have been shown to affect the final particle size and morphology. For example, Li et al. analyzed the influence of temperature, ion strength, and pH on the well-known citrate-mediated synthesis of AuNPs.[32] They found that a decrease in the reaction temperature allowed a higher control over the nucleation rate. In addition, they established that the particle size distribution could be influenced by pH-dependent growth mechanisms, which was attributed to differences in colloidal stabilities of particles based on their average size and surface potential, as determined by electrophoresis. Briñas et al. developed a method for size-controllable Au colloids on the basis of the formation of $Au^+$-glutathione polymeric NP precursors, which change size and density depending on the pH.[33] Wang et al. also studied the pH-dependent speciation of aqueous $HAuCl_4$ and its influence on the synthesis of AuNPs. Using ascorbic acid and sodium benzenesulfonate as reducing and capping agents, respectively, the reduction of $HAuCl_4$ at low pH led to the synthesis of well-dispersed and uniform AuNPs, whereas at high pH, large Au colloids and ensembles of small Au colloids were formed.[34]

Alternatively to the seedless synthesis, the seed-mediated approach has been proposed for precise control over the size and shape of NPs.[35,36] Dating back to the 1920s, it is well accepted as the most efficient and controlled methodology for the targeted synthesis of NPs with various morphologies.[37] This method involves the separation of the nucleation and growth events. First, premade seeds of well-defined size and (crystallographic) shape are added to a growth solution containing a metal salt precursor and a mild reducing agent. In the growth step, the metal salt precursor will be catalytically reduced on the seeds. Here, the final particle size can be controlled by the molar ratio of a metal precursor to seeds available in the growth solution, normally denoted *R*, that is, [metal precursor]/[metal seed]. At the same time, the final nanocrystal shape can be controlled by either the crystalline structure of the initial seed, the presence of shape-directing ligands, and/or other additives. For example, Jana et al. studied the seed-mediated growth of citrate-stabilized AuNPs (12 nm) for a wide range of reducing agents and conditions.[36] Rodríguez-Fernández et al. reported the seed-mediated growth of CTAB-stabilized Au spheres from 15 nm to sizes from 60 up to 180 nm within narrow size distributions.[35] Sánchez-Iglesias et al. have shown how a thermal-induced seed optimization allowed the high-yield synthesis of monodisperse, pentatwinned gold nanorods, decahedra, and bipyramids with a great control over the final dimensions.[38]

For the synthesis of Au triangular prismatic NPs, the range of available approaches can be divided into two main mechanisms, namely, "plate-like" and "face-blocking" growth.[39−41] Plate-like growth builds on twinned seeds with stacking faults (coalescent {111} facets). Because the growth along the reentrant grooves is highly favored, nanotriangles of low thickness (<10 nm) in a wide range of aspect ratios (from 5 up to >20) are accessible.[42−48] However, common approaches report low control over the size dispersity and low initial shape yield of 30−40%, especially in the sub-200-nm size range.[30] Face-blocking growth describes the directed growth upon selective adsorption of surfactants to most-favorable facets (capping). By this "surfactant-templating", the overgrowth of single-twinned seeds to nanotriangles of lower aspect ratio (<5) was initially proposed by Mirkin et al.[49] and later improved by Scarabelli et al.[30] They showed that an initial shape yield above 50% can be achieved by a two-step approach: (1) generation of CTAC-capped single-twinned seeds (<10 nm) and (2) "fast seed addition" to a growth solution using ascorbic acid, yielding nanotriangles between 60 and 150 nm after depletion-induced purification. This phenomenon has been explained by the presence of iodide ions during the fast overgrowth of the seed, which fosters seed twinning[50] and that iodide is crucial for the required symmetry-breaking.[51] However, the proposed method cannot be applied to overgrow preformed triangles as the high etching power of ascorbic acid causes a dulling of the tips/edges, ultimately yielding spherical morphologies. To the best of our knowledge, a seed-mediated approach that enables a controlled overgrowth using Au nanotriangles as "large" seeds has not been reported.

Alternatively, we have recently proposed a seedless method for the synthesis of AuNTs using 3-butenoic acid (3BA) in the presence of benzyldimethylammonium chloride (BDAC) as a capping agent (step 1 in Scheme 1).[52] 3BA is a mild reducing agent unable to reduce $AuCl_4^-$ ions to $Au^0$ at room temperature. Thus, to promote nucleation,[52] the reducing capabilities of 3BA need to be increased by elevated temperatures[53] or increased pH values. The sequential reduction of $Au^{3+}$ to $Au^+$ and finally to $Au^0$ is accompanied by Tsuji−Wacker oxidation of 3BA upon the formation of succinic semialdehyde or acetoacetic acid (see Scheme S1).[54]

**Scheme 1. Two-Step AuNT Synthesis Using the 3BA Approach with BDAC[a]**

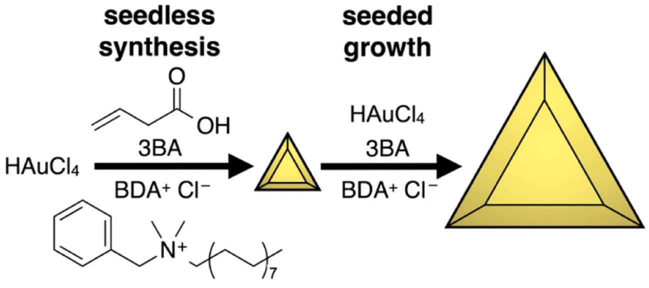

[a] Step 1: seedless synthesis of well-defined AuNTs as "large seeds" (30−55 nm edge length) for further overgrowth. Step 2: seed-mediated growth of AuNTs (100−180 nm edge length) retaining their truncated triangular bipyramid morphology.

Gómez-Graña et al. suggested that 3BA favors thermodynamic controlled growth, stabilizing preferably {111} facets.[53] In this "one-pot" nucleation-growth process, two principal kinds of nuclei may form, namely, single-crystalline and twinned seeds. Thus, upon thermodynamic controlled growth, single crystals form octahedra (NOCs, enclosed by 8 {111} facets). Single-twinned seeds grow into triangular bifrustums,[55] that is, truncated triangular bipyramids ({111} facets on top/bottom), which are simply referred to as triangles (NTs), and pentatwinned seeds form decahedra (enclosed by 10 {111} facets). Consequently, the 3BA approach results in dispersions composed of a mixture of AuNTs and gold nanooctahedra (AuNOCs) with a minor amount of byproducts (Au decahedra and larger morphologies), as previously reported.[52] By depletion-induced separation,[56] both AuNTs and AuNOCs can be purified and isolated. In addition, 3BA grants access to chemical postfunctionalization, for example, by free-radical polymerization. The vinyl functionalities enable a direct encapsulation of nanoparticles by a polymer shell such as pNIPAM, p4VP, or PS without the requirement of an additional step for the surface modification.

Here, we show that the AuNTs obtained by the seedless 3BA approach can serve as large seed particles (30−55 nm in edge length) for further Au overgrowth, giving access to the sub-200-nm size range (step 2 in Scheme 1). First, we address the 3BA-mediated synthesis of AuNT seeds, investigating the three main control parameters for a control over size and shape yield: temperature, solution pH, and concentration of the reducing agent. Then, we demonstrate the seed-mediated growth of AuNTs between 100 and 180 nm in edge length and 50 and 80 nm in thickness, with a constant low aspect ratio of about 2.1. To the best of our knowledge, this is the first time that well-defined gold triangles can be overgrown retaining their well-defined truncated triangular bipyramid morphology. The evolution of the NT morphology upon growth, including edge length, thickness, and edge rounding, is quantified by a combination of electron microscopy (transmission electron microscopy (TEM) and field-emission scanning electron microscopy (FESEM)) and small-angle X-ray scattering (SAXS). We show that the tip sharpness is maintained throughout the overgrowth, which is an indicator of the NT quality and essential for application in SERS. Finally, we investigate the size-dependent SERS enhancement of the overgrown AuNTs in dispersion by quantification of the analytical enhancement factors (AEFs) and the limit of detection using 4-mercaptobenzoic acid (4MBA) as a model analyte.

## EXPERIMENTAL SECTION

**Materials.** Sodium hydroxide in pellets (>98%), 3-butenoic acid (3BA, 97%), cetyltrimethylammonium chloride (CTAC, ≥98%), benzyldimethylhexadecylammonium chloride (BDAC, ≥97%), cetyltrimethylammonium bromide (CTAB, ≥98%), and $HAuCl_4 \cdot 3H_2O$ (≥99.9% trace metal basis) were supplied by Sigma. 4-Mercaptobenzoic acid (4MBA, >95%) was purchased from Tokyo Chemical Industry (TCI). All reactants were used without further purification. Water was purified using a Milli-Q system (Millipore).

**Characterization Methods.** UV−vis−NIR measurements of aqueous colloidal solutions were recorded with an HP Agilent 8453 diode array spectrophotometer. Transmission electron microscopy (TEM) images were obtained by a JEOL JEM 1400 operating at an acceleration voltage of 80 kV. TEM samples were prepared by drying a 10 $\mu$L drop of a colloidal suspension of AuNTs, where the excess surfactant was removed by two centrifugation and redispersion cycles, on a carbon-coated copper grid. Field-emission scanning electron microscopy (FESEM) images were obtained by a FEI Helios Nanolab 650 Dual Beam working at an acceleration voltage of 15 kV and a current intensity of 0.2 nA. FESEM samples were prepared by drying 20 $\mu$L of an aqueous colloidal solution of AuNTs with a particle concentration of $[Au^0]$ ∼1 mM and 1.5 mM CTAB on a 1 × 1 $cm^2$ polished boron-doped silicon (111) wafer.

Small-angle X-ray scattering (SAXS) data were recorded using a "Double Ganesha AIR" (SAXSLAB, Denmark). The X-ray source of this laboratory-based system is a rotating anode (copper, MicoMax 007HF, Rigaku Corporation, Japan) providing a parallel beam at $\lambda$ = 0.154 nm. The measurements were carried out on samples contained in 1 mm glass capillaries (Hilgenberg, code 4007610, Germany) at room temperature, and the transmitted intensity data were recorded by a position-sensitive detector (PILATUS 300 K, Dectris). To cover the range of scattering vectors between 0.02 and 5.0 $nm^{-1}$, different detector positions were used. The circularly averaged data were normalized to incident beam, sample thickness, and measurement time before subtraction of the solvent. All measurements were put on an absolute scale by standardless absolute intensity calibration.

Surface-enhanced Raman scattering was recorded with a confocal Raman microscope (WiTec GmbH, Ulm, Germany) equipped with a 300 grooves/mm grating, a Peltier-cooled charge-coupled device camera, and a 785 nm laser (30 mW) as an excitation line. A HeNe laser was used for reference measurements at 633 nm excitation (see Figure S19). Spectra were recorded by focusing the laser spot below the air/liquid interface of the sample liquid (200 $\mu$L) using a 10× objective lens (Zeiss, NA 0.2), providing a spatial resolution of ∼2 $\mu m^2$. Each sample was measured at least three times, and time-series data (300 spectra × 1 s exposition) was accumulated for the final spectra. The equimolar sample solutions were prepared from aliquots of CTAB-stabilized NT dispersions ($[Au^0]$ = 0.25 mM, [CTAB] = 0.5 mM) and aqueous analyte solutions ([4MBA] = 1 $\mu$M; 11 vol % EtOH). For spectral assignment, SERS data was evaluated in reference to spectra of bulk materials (4MBA, CTAB, BDAC, and EtOH) and reference analyte solutions of known concentrations ([4MBA] = 0.1, 0.05, and 0.01 M) obtained by conventional volume Raman spectroscopy. Data analysis and background correction were done by multipeak fitting using Igor Pro 7 (WaveMetrics, Inc.).

**Synthesis at Different Temperatures.** AuNTs and AuNOCs were synthesized by following a similar procedure reported recently.[52] In a typical synthesis, 50 mL of an aqueous mixture containing 0.5 mM $HAuCl_4$ and 5 mM BDAC was introduced into a two-neck round-bottomed flask under mild magnetic stirring. After that, the solution was heated to the desired temperature (70, 75, 80, 85, 90, or 95 °C). Then, 100 $\mu$L of 3BA (11.4 M) was added, reaching a final [3BA] = 22.8 mM and a $[3BA]/[HAuCl_4]$ ratio of 45.6. The complete reduction of available $HAuCl_4$ to $Au^0$ was confirmed by UV−vis analysis, and the solution was allowed to cool down to RT. Finally, the excess of 3BA and BDAC was removed by centrifugation at 5500 rcf (relative centrifugal force) for 30 min in every case. The supernatant was discarded, and the pellet was redispersed in 50 mL of 4 mM BDAC.

**Synthesis at Different pH Values.** For the synthesis at several pH values, at a selected temperature of 75 °C and keeping constant the amounts of BDAC (5 mM) and 3BA (100 $\mu$L), different amounts of a 1 M NaOH solution were added into the reaction mixture (0, 25, 50, 75, 100, 200, 400, and 800 $\mu$L corresponding to pH values of 5.7, 6.1, 6.8, 7.5, 8.2, 9.3, 10.5, and 12.5, respectively). In a typical synthesis, 50 mL of a mixture containing 0.5 mM $HAuCl_4$ and 5 mM BDAC was heated to 75 °C. Then, 25 $\mu$L of 1 M NaOH was added under mild magnetic stirring. Immediately after that, 100 $\mu$L of 3BA was added into the mixture, which was left to react until all of the $HAuCl_4$ was reduced to $Au^0$, as confirmed by UV−vis analysis. The solution was allowed to cool down to RT, and the excess of 3BA and BDAC was removed by centrifugation at 5500 rcf for 30 min in every case. Finally, the supernatant was discarded and the pellet was dispersed in 50 mL of 4 mM BDAC.

**Purification of AuNTs.** For particle separation, the mixture of AuNTs and AuNOCs was purified by the depletion-induced

**Table 1. Summary of Molar Ratio $R$, Seed Concentration $[Au^0]$, Concentration of Gold Precursor Salt, Average Thickness $T_{FESEM}$, and Edge Length $L_{TEM}$ Evaluated by FESEM and TEM Image Analysis, Average Thickness $T_{SAXS}$ and Edge Length $L_{SAXS}$ Determined by SAXS, Difference in Edge Lengths $\Delta L$ ($=L_{SAXS} - L_{TEM}$), Tip Rounding $s_{tip}$, and LSPR Extinction Maxima for AuNTs of Increased Sizes Obtained from Au Overgrowth**

| $R$ | $[Au^0]$, mM | $[HAuCl_4]$, mM | $L_{TEM}$, nm | $T_{FESEM}$, nm | $T_{SAXS}$, nm | $L_{SAXS}$, nm | $L_{SAXS} - L_{TEM}$, nm | $s_{tip}$, % | LSPR, nm |
|---|---|---|---|---|---|---|---|---|---|
| seeds | | | 54.8 ± 4.0 | 33.0 ± 3.4 | 32 ± 2.3 | 75 ± 3.8 | 20.2 ± 5.5 | 15.6 ± 4.9 | 591 |
| 2.5 | 0.055 | 0.1375 | 86.3 ± 4.0 | 52.4 ± 4.2 | 50 ± 1.5 | 105 ± 3.2 | 18.7 ± 5.2 | 10.3 ± 3.2 | 617 |
| 5 | 0.055 | 0.275 | 103.6 ± 4.2 | 62.0 ± 4.3 | 58 ± 8.7 | 130 ± 9.1 | 26.4 ± 10.0 | 11.7 ± 5.3 | 633 |
| 7.5 | 0.055 | 0.4125 | 128.1 ± 5.2 | 70.8 ± 3.2 | 68 ± 10.2 | 145 ± 5.8 | 16.9 ± 7.8 | 6.7 ± 3.4 | 669 |
| 10 | 0.055 | 0.55 | 137.0 ± 4.5 | 74.7 ± 2.9 | 72 ± 9.4 | 157.5 ± 14.2 | 20.5 ± 14.9 | 7.5 ± 6.2 | 684 |
| 15 | 0.055 | 0.825 | 173.7 ± 7.1 | 81.4 ± 5.1 | 80 ± 12.0[a] | 162.5 ± 11.4[a] | [a] | [a] | 742 |

[a] SAXS values of the largest NTs ($R$ = 15) are affected by particle sedimentation owing to a limited colloidal stability over the integration time.

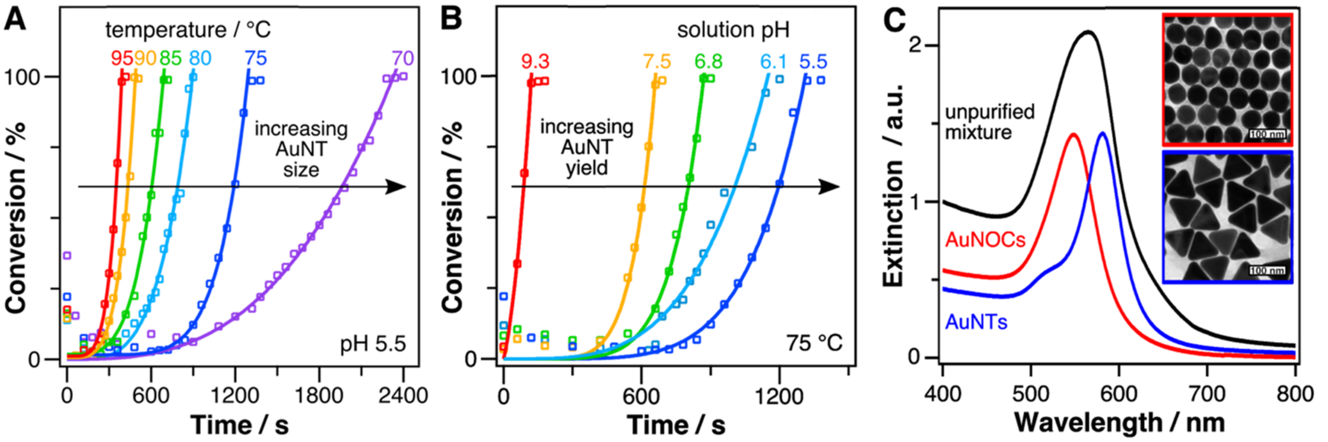

**Figure 1.** Synthesis of AuNT seed particles: (A) temperature-dependent and (B) pH-dependent conversion kinetics of Au precursor to $Au^0$ by time-resolved UV−vis spectroscopy. The lines are a guide to the eye. (C) Extinction spectra of unpurified as-synthesized seed mixture (black: 75 °C, pH 5.5) and after purification by depletion-induced separation: purified AuNTs (blue) and purified AuNOCs (red).

separation approach using CTAC at room temperature.[56] The concentration of CTAC was varied as a function of the AuNT size. For instance, the as-synthesized particles at 75 °C were centrifuged at 5500 rcf for 30 min. The supernatant was discarded, and the precipitate was redispersed in a 5 mL vial containing 2 mL of 100 mM CTAC. After 4 h at room temperature, the precipitate formed at the bottom of the vial was discarded. The supernatant, containing a mixture of AuNTs and AuNOCs, was again centrifuged at 5500 rcf for 30 min. The supernatant was discarded, and the precipitate was redispersed in a 5 mL vial containing 2 mL of 175 mM CTAC. After 4 h, the supernatant, containing AuNOCs, was separated, and the precipitate formed at the bottom of the vial, containing AuNTs, was redispersed in 10 mL of 5 mM BDAC.

**Seed-Mediated Gold Overgrowth.** For the overgrowth, purified AuNTs synthesized at 75 °C were used as seeds. The initial $HAuCl_4$ concentrations were calculated to obtain different molar ratios, $R$ ($[HAuCl_4]/[Au^0]$ = 2.5, 5, 7.5, 10, and 15), while the concentration of seeds was kept constant ($[Au^0]$ = 0.055 mM). For a typical synthesis, for example, $R$ = 2.5, the growth solution containing 44.53 mL of 0.1375 mM $HAuCl_4$ and 5 mM BDAC was heated to 70 °C. Then, 50 $\mu$L of 3BA (11.4 M) was added under mild magnetic stirring for $[3BA]/[HAuCl_4]$ ratios of 82.9, 41.5, 27.6, 20.7, and 13.8. When the mixture became colorless, 5.47 mL of AuNTs ($[Au^0]$ = 0.63 mM) was added. The solution was stirred at 100 rpm (70 °C) for 1 h. Finally, the excess of 3BA and BDAC was removed by centrifugation at 4500 rcf for 30 min. The supernatant was discarded, and the pellet was redispersed in 5 mM BDAC. Table 1 shows a summary of the synthesis parameters as well as the final size of AuNTs.

## ■ RESULTS AND DISCUSSION

**AuNT Seed Synthesis: Influence of Temperature, pH, and the Reducing Agent Concentration.** For the synthesis of large AuNT seeds (>30 nm), we applied an approach based on 3BA as a reducing and shape-inducing agent, as recently reported (step 1 in Scheme 1).[52] Because 3BA can be considered as a mild reducing agent, it will not be able to reduce $Au^{3+}$ salt to $Au^0$ at room temperature. Thus, the reducing power of 3BA could be increased by increasing either the temperature or basic pH values. To find ideal conditions for controlling size and yield of AuNT seeds, we tested different temperatures and pH values (see Figure 1). The total conversion of $Au^{+3}$ to $Au^0$ was monitored by time-resolved UV−vis spectroscopy on the basis of the molar extinction of $Au^0$ at 400 nm as a reference.[57,58] Figure 1A shows that the conversion rate dramatically depends on the temperature (between 40 min at 70 °C and 7 min at 95 °C, see Section SI.1 and Figures S1−S3). The temperature-dependent reducing power of 3BA determines the balance between the nucleation and growth processes. Consequently, AuNT seed size can be controlled by temperature. We found a linear correlation between edge length $L$ and temperature $t$, which enables the seedless fabrication of size-tailored AuNTs in a controlled manner (see Figure S4, $L/\text{nm} = 132 - 1 \times t/°\text{C}$). Figure 1B shows that the conversion speed also depends on the pH of the precursor solution. By addition of NaOH, the conversion speed can be adjusted (between 22 min at pH 5.5 and 2 min at pH 9.3, see Section SI.2 and Figure S5). However, the yield of AuNT seeds was found to decrease with the increasing pH (see Figure S6). Above pH 9.3, the yield is dramatically reduced and the AuNT shape is almost completely lost. The yield of mainly spherical NPs indicates a pH-induced transition from

DOI: 10.1021/acsami.7b19081
ACS Appl. Mater. Interfaces 2018, 10, 11152−11163

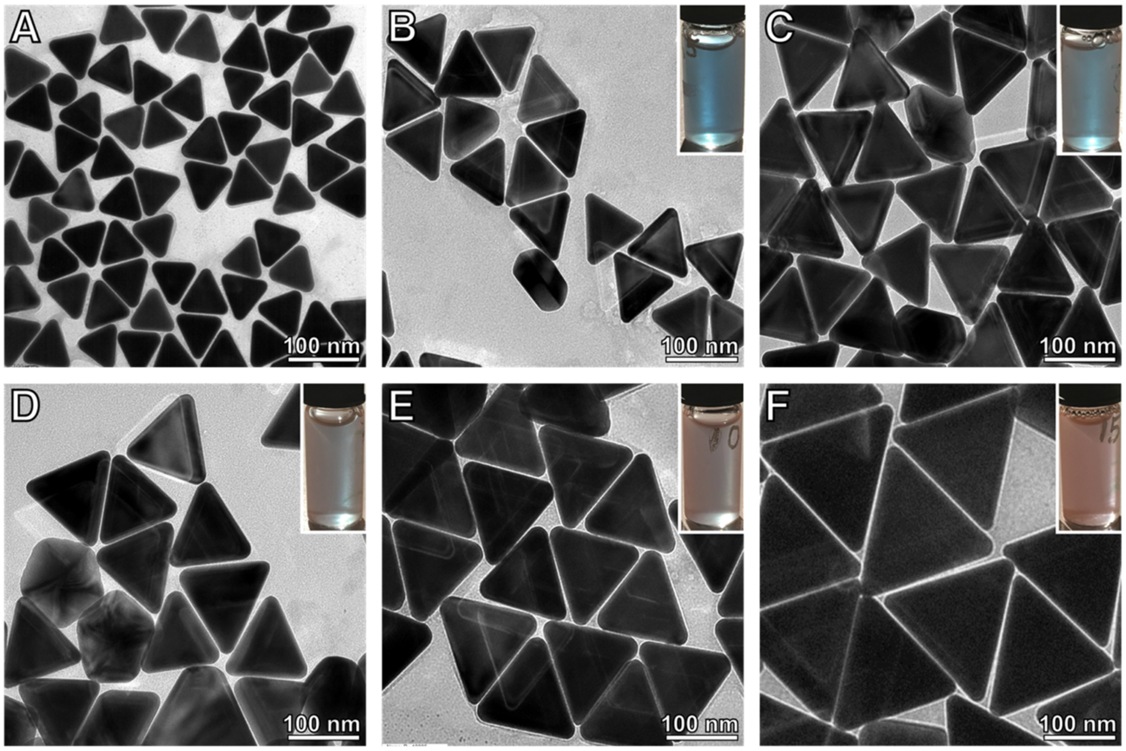

**Figure 2.** TEM images of horizontally oriented AuNTs before (A) and after Au overgrowth at different ratios (*R*): 2.5 (B), 5 (C), 7.5 (D), 10 (E), and 15 (F). Inset photographs show the optical transmission.

thermodynamic to kinetic control. Like temperature, the pH determines the reducing power of 3BA and consequently controls the size of resulting AuNT seeds. Within a limited pH range of 5.5−9.3, the edge length scales linearly with pH (see Figure S7, $L/\text{nm} = 82 - 5 \times \text{pH}$). Thus, by pH, the AuNT seed size can be tuned between 55 and 30 nm, however, considering a reduced yield of AuNTs.

We have also tested the influence of the reducing agent concentration at 75 °C by analyzing different $[3BA]/[HAuCl_4]$ ratios ranging from 11.4:1 to 91.2:1 (see Figure S8). The obtained results were the same in all cases, which are as follows: (i) no reaction takes place at room temperature; (ii) an increase in the reaction temperature above 60 °C is needed to trigger the nucleation process; and (iii) a mixture of triangular, octahedral, and decahedral particles of similar percentages was obtained. On the other hand, the presence of a higher concentration of reducing agent led to a decrease in the reaction time from 110 to 80 min when the $[3BA]/[HAuCl_4]$ ratio was increased from 11.4:1 to 91.2:1. Therefore, we can conclude that the $[3BA]/[HAuCl_4]$ ratio affects only the kinetics of the process but not the actual yield of differently shaped products.

For the overgrowth, we selected AuNT seeds synthesized at 75 °C and at pH 5.5. These conditions yield AuNTs with an edge length of 55 ± 4 nm at a maximum yield of approximately 50% (as estimated from TEM images). Figure 1C shows the UV−vis spectra of the unpurified as-synthesized seed mixture (black) with a broad LSPR band at 566 nm. The AuNT seeds were separated by depletion-induced purification using 0.175 M CTAC.[56]

We used CTAC because the surfactant-induced separation can be performed at room temperature without additional heating. In the case of using BDAC or CTAB, we have observed that surfactant precipitation would necessitate heating of the solution during depletion flocculation. In the pioneering work of Park et al.,[56] CTAB/BDAC mixtures have been reported. They observed that BDAC dominates the overall properties over most of the mole fraction range because BDAC forms micelles at a lower critical concentration than that of CTAB as well as because of differences in aggregation numbers (micelle size). Consequently, this results in a greater depletion potential for a BDAC solution than for a CTAB solution at the same absolute surfactant concentration. Liz-Marzán et al. applied CTAC for the purification of AuNTs,[30] using the equation proposed by Park et al. In principle, the molar concentration of the surfactant and the critical micelle concentration are the determining parameters. We want to emphasize, using BDAC instead of CTAC, that it would be necessary to change the surfactant concentration accordingly as well as provide additional heating during flocculation.

After purification, the supernatant containing AuNOCs exhibited a LSPR at 548 nm (Figure 1C, red), whereas the precipitate containing AuNTs showed a narrow main (in-plane, longitudinal) mode at 591 nm and a second (out-of-plane, transversal) mode at 520 nm as a shoulder (Figure 1C, blue).[59]

**Au Overgrowth of AuNT Seeds.** Next, the purified AuNT seeds were overgrown, retaining their shape, by reducing $HAuCl_4$ with 3BA in the presence of BDAC (step 2 in Scheme 1; see Experimental Section for details). Once all of the $AuCl_4^-$ was reduced to $AuCl_2^-$, the purified AuNT seeds were added to promote the catalytic reduction of $AuCl_2^-$ at their surface. In this way, the size of the AuNTs was increased, whereas their triangular shape was maintained. This process allowed the preparation of monodisperse AuNTs with a range of sizes by simply varying the molar ratio of $HAuCl_4$ to AuNT seeds (*R*). Figure 2 shows representative TEM images of AuNTs obtained at high yield with different *R* values (2.5, 5, 7.5, 10, and 15), indicating an increase in the edge length of AuNTs with *R* (see

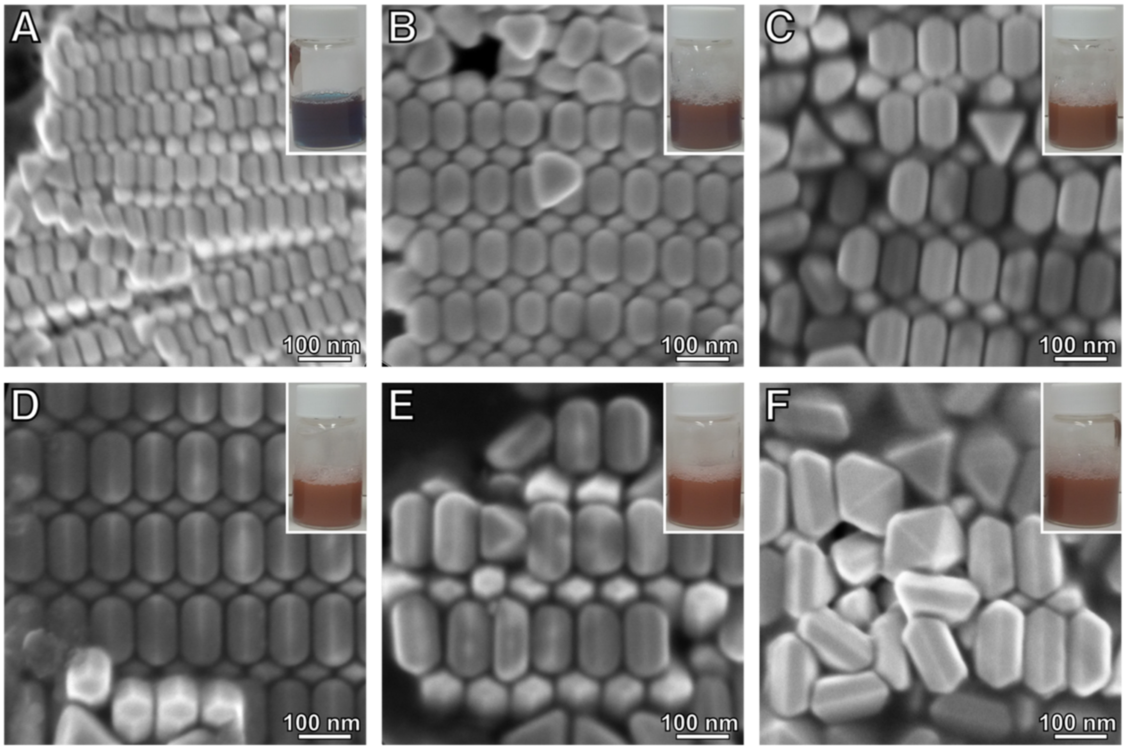

**Figure 3.** FESEM images of vertically oriented AuNTs before (A) and after Au overgrowth at different ratios ($R$): 2.5 (B), 5 (C), 7.5 (D), 10 (E), and 15 (F). Inset photographs show the optical reflection.

also Figure S11 for low-magnification images). It should be pointed out that the overgrowth process of the purified AuNTs was performed at a constant concentration of the reducing agent ([3BA]/[$HAuCl_4$]).

As the first step, the overgrown particles were analyzed by TEM and FESEM to quantify the increase in the edge length and thickness after each overgrowth step. The TEM data clearly shows an increase in the average edge length ($L_{TEM}$) from 55 ± 4 nm (seeds) to 86 ± 4 nm for the lowest overgrowth relationship ($R$ = 2.5) and up to 174 ± 7 nm for the highest overgrowth relationship ($R$ = 15) (see Figure S12). To quantify the AuNT thickness, we also performed tilted TEM imaging. Figure S13 shows exemplary TEM images for several $R$ values at tilting angles of 0 and 60°. Unfortunately, we need to point out that the tilting angle is limited to ±60°. Consequently, a full 90° tilt, which would give access to directly measure the AuNT thickness, is not possible. Thus, the thickness cannot be accurately resolved by tilted TEM.

Alternatively, the average thickness ($T_{FESEM}$) was evaluated by FESEM image analysis of closely packed layers of vertically oriented AuNTs (Figure 3).[60,61] The thickness increased from 33 ± 4 nm (seeds) to 53 ± 3 nm for the thinnest overgrowth ($R$ = 2.5) and up to 82 ± 3 nm for the thickest overgrowth ($R$ = 15) (see Figure S14). Figure 3 shows representative SEM images of NTs assembled at relatively high surfactant concentrations (see Experimental Section), leading to assemblies of vertically oriented particles in an alternating (honeycomb) configuration.[60] In summary, this methodology allows us to obtain monodisperse AuNTs with a tight size control in a size range of 55−175 nm in the edge length and 30−80 nm in thickness (see Table 1).

The plasmonic properties of AuNTs are influenced by several morphological parameters including edge length, thickness, and tip rounding. Figure 4 shows the schematic representation of the NT morphology at different stages of the overgrowth: with the lowest overgrowth relationship $R$ = 2.5 (A, yellow) and the highest overgrowth relationship $R$ = 15 (B, orange). However, an analysis of the morphological parameters by electron microscopy image analysis is statistically challenging and cumbersome, which is especially true for the evaluation of the tip/edge rounding. For this purpose, we performed small-angle X-ray scattering (SAXS) to characterize the NT morphology. SAXS has been recently applied to investigate the time-dependent Ostwald ripening growth mechanism of NTs using a simple analytical model of a homogeneous cylinder/disk as a first-order approximation of the NT's thickness and radius of gyration.[46]

Here, we use an alternative approach based on three-dimensional (3D) atomistic modeling, which allows the characterization of highly anisotropic and complex morphologies.[14,62] The model consists of 30 000 scattering centers randomly placed within the boundaries set by the idealized NT geometry of a triangular bifrustum,[55] that is, a symmetrically truncated triangular bipyramid (see Section SI.4 and Figure S15). The model consists of beveled sides[43] (protruded {100} facets) at an angle of 120°, as indicated by FESEM.[44] The SAXS analysis considers sharp tips unaffected by edge rounding, for which edge length $L_{SAXS}$ is defined by the total tip-to-tip distance. In the SAXS model, the tip and edge rounding can be neglected because the NT dimensions (volume) are the most dominant scattering contributions in the observed $q$-range of 0.025−1 $nm^{-1}$, as discussed recently.[14] Figure 4C shows the SAXS scattering curves (gray) fitted by the 3D model (black) over the experimentally measured $q$-range (for details, see Figure S16). The best fit was determined by a brute-force approach for which all combinations of the four independent parameters (edge length, dispersity in edge length, thickness, and dispersity in thickness) were systemati-

DOI: 10.1021/acsami.7b19081
ACS Appl. Mater. Interfaces 2018, 10, 11152−11163

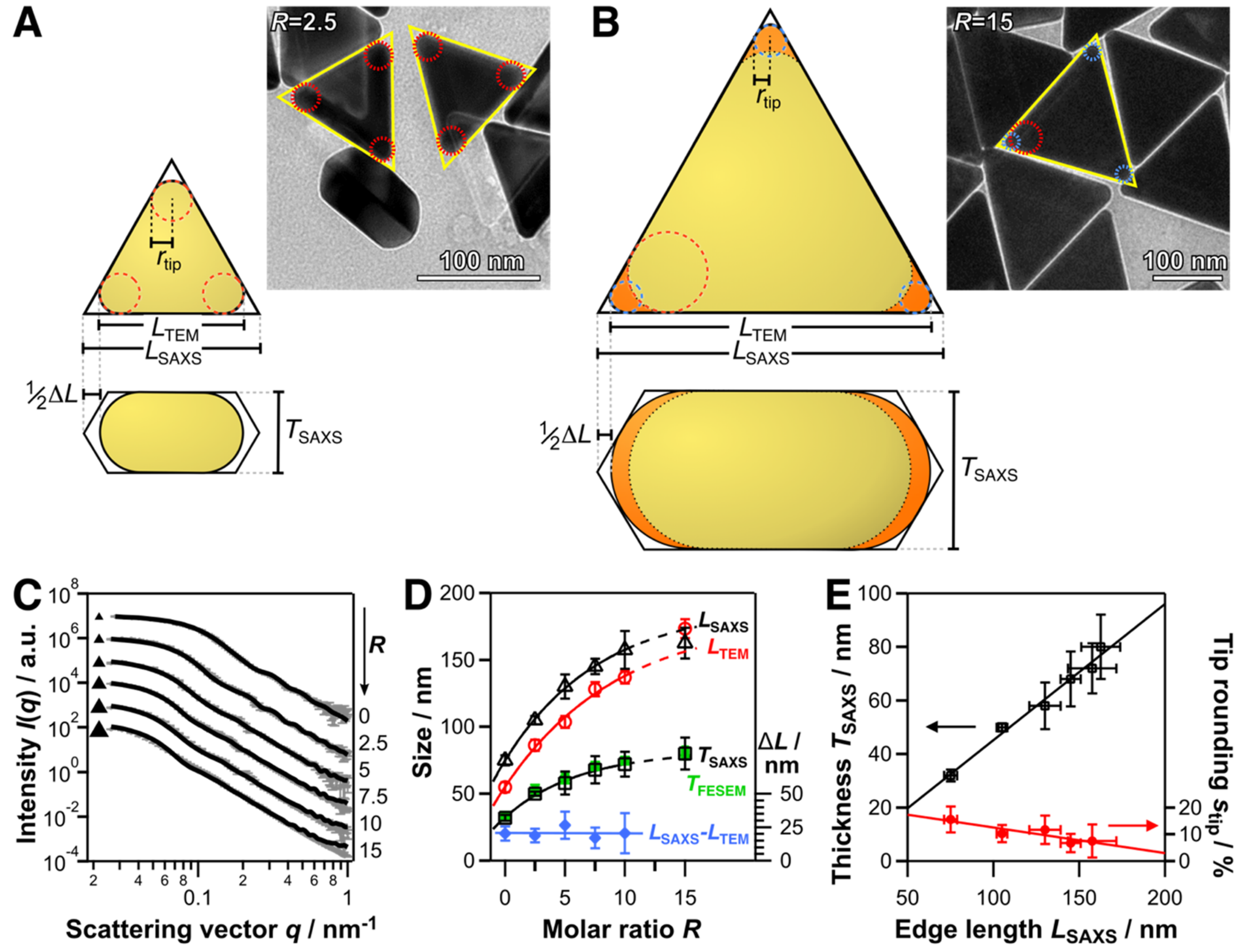

**Figure 4.** Morphological characterization of AuNTs from the colloidal dispersions by small-angle X-ray scattering. Schematic representation of the NT dimensions and shapes for different stages of the overgrowth process: (A) thin overgrowth with $R = 2.5$ and (B) thick overgrowth with $R = 15$ (TEM insets highlight the differences in tip rounding). The dashed circles in red ($R = 2.5$) and blue ($R = 15$) colors indicate the respective tip curvature, $r_{tip}$. (B) Differences in tip/edge sharpness (orange) of the largest AuNTs by direct comparison with the smaller AuNTs (A), scaled to the same size. (C) Experimental scattering signatures (gray dots) and simulations (black lines) for different molar ratios $R$ (offset applied for clarity). (D) Size parameters evaluated by SAXS (black), TEM (red), FESEM (green), and differences in edge lengths $\Delta L$ (blue) owing to edge rounding. The lines are a guide to the eye. (E) Linear correlation of edge length and the thickness indicating the controlled Au overgrowth (black) and evolution of tip rounding $s_{tip}$ (red) with the increase in size.

cally calculated. The simulation resulted in four-dimensional maps, in which the best fit was selected by comparison of the mean-squared error with the complete experimental scattering profile. Figure 4D shows ensemble-averaged thickness $T_{SAXS}$ and edge length $L_{SAXS}$, as determined by SAXS (see also Table 1). The high agreement of the thickness values obtained from FESEM (green) and SAXS (black) further proves that the SAXS modeling is accurate (Figure S17). The linear correlation of the edge length and thickness indicates a controlled overgrowth (black) depending on the amount of available Au precursor (Figures 4E and S14). As expected, the SAXS-evaluated edge lengths, $L_{SAXS}$, (black) differ from the TEM results, $L_{TEM}$, (red) and exhibit a constant offset ($\Delta L = L_{SAXS} - L_{TEM}$) of 17−26 nm (blue), which originates from tip/edge rounding (Figure 4D). The rounding of the NT tips, $s_{tip}$, is defined by the local radius of curvature, $r_{tip}$, (compare Figure 4A,B) scaled by the total edge length.[16] By simple geometric considerations (see Section SI.4), $s_{tip}$ can be calculated from the differences in edge lengths $\Delta L$. Figure 4E shows the evolution of tip rounding with the increasing size (red). Because the radius of curvature remains almost constant (10−15 nm) for all sizes, the tip rounding decreases for the increasing NT sizes. Consequently, the tip sharpness was maintained throughout the overgrowth, which is an indicator of the NT quality and essential for application in SERS.

Next, we address the impact of the overgrowth on the optical properties, for which two opposing effects take place: (1) an increase in the edge length causes a red shift of the main LSPR mode and (2) an increase in the thickness correlates to a blue shift (truncation) of the main LSPR mode.[63] Consequently, a concomitant growth in lateral and transversal direction by Au overgrowth will result in an extenuated linear red shift and a broadening of the main LSPR band. Figure 5A shows the UV−vis spectra of AuNTs obtained with different $R$ values. Both red-shifting and broadening of the LSPR band can be clearly observed for increasing $R$ values. The seed LSPR peak at 591 nm initially shifted to 617 nm for small AuNTs ($R = 2.5$) and subsequently shifted toward the NIR for large AuNTs ($R = 15$)

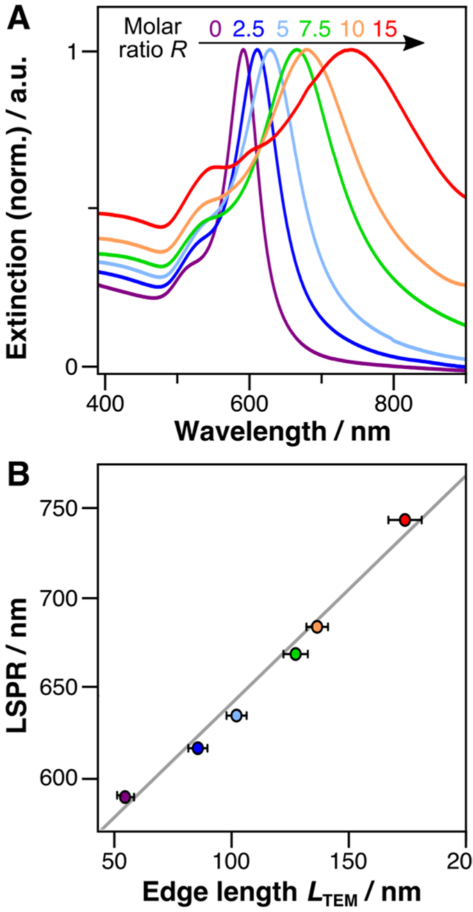

**Figure 5.** (A) Normalized absorbance spectra of AuNTs before (violet line) and after seed-mediated Au overgrowth for different molar ratios *R*: 2.5 (dark blue), 5 (light blue), 7.5 (green), 10 (orange), and 15 (red). (B) Linear shift of the LSPR maximum with the increasing size.

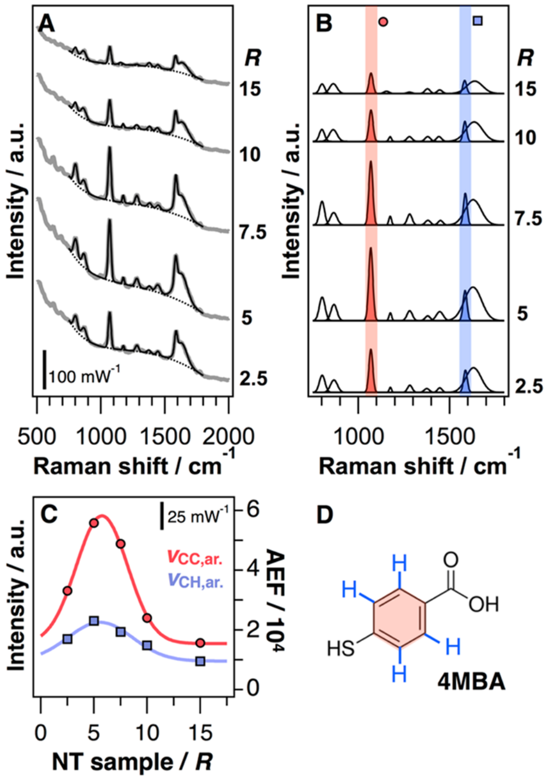

**Figure 6.** SERS performance of differently sized AuNTs in solution. (A) SERS spectra at constant concentrations of Au (0.25 mM), CTAB (0.05 mM), and 4MBA (1 $\mu$M) excited at 785 nm (offset applied for clarity; before background correction). (B) Relative signal intensities of the breathing mode ($\nu_{\mathrm{CC,ar.}}$, 1070 cm$^{-1}$, red circles) and axial ring deformation ($\nu_{\mathrm{CH,ar.}}$, 1580 cm$^{-1}$, blue squares) of the aromatic phenyl ring evaluated by spectral deconvolution. (C) Analytical enhancement factors (AEFs): The AuNTs of *R* = 5 and 7.5 yield the highest enhancement at 1070 cm$^{-1}$ ($\nu_{\mathrm{CC,ar.}}$) and 1580 cm$^{-1}$ ($\nu_{\mathrm{CH,ar.}}$) corresponding to the aromatic vibrations of 4MBA (D). The lines serve as a guide to the eye.

at 742 nm (see Table 1). The linear dependence between the AuNT size and the LSPR maximum in the visible range was initially reported by Scarabelli et al.[30] using a different synthetic approach and is in complete agreement with our findings using the 3BA approach (see Figure 5B).

**SERS Performance.** Next, we investigated the SERS performance of the prepared AuNTs for the ultrasensitive detection of molecular traces. For benchmarking, we selected 4-mercaptobenzoic acid (4MBA) as a low-molecular-weight aromatic ligand with high binding affinity for metal surfaces. The choice of CTAB for the SERS measurements was based on several reasons: First, CTAB serves as a stabilizing agent to avoid particle aggregation and aggregation-induced SERS enhancement. Second, CTAB is a nonaromatic surfactant with low Raman cross section and low spectral background. Third, in earlier studies, we already addressed the topic of CTAB detection on gold nanoparticles; thus, the vibrational signals of CTAB were well-known.[70] The detection and removal of surfactants and molecular contaminants (e.g., from synthesis) are vital for a controlled particle surface chemistry and are required for many applications.

By comparison of equimolar NT samples (in terms of gold), each containing 0.25 mM Au$^0$ and 1 $\mu$M 4MBA, the different SERS enhancements at 785 nm excitation were probed. The obtained spectra are rich in information (Figure 6A) and can be readily evaluated by multipeak fitting (Figure 6B). The spectral background cannot be attributed to either the fluorescence of 4MBA or any other chemical component of the NP dispersion. To the best of our knowledge, it does not originate from the NP dispersions but might be related to optical components of the Raman setup because the same background was found for pure water (Figure S20A,B).

The highest signal intensities can be found for the breathing mode ($\nu_{\mathrm{CC,ar.}}$, 1070 cm$^{-1}$, red circles) and axial ring deformation ($\nu_{\mathrm{CH,ar.}}$, 1580 cm$^{-1}$, blue squares) corresponding to the phenyl ring of 4MBA.[64] The CS stretching (513 and 625 cm$^{-1}$) and carboxyl bending and stretching signals (800, 870, 1180, 1280, and 1440 cm$^{-1}$) are detectable but less pronounced.[65] The broad signal at 1630 cm$^{-1}$ can be attributed to the bending vibration of $H_2O$.[66]

In retrospect, it is likely that a fair share of SERS studies in the literature might be affected by particle aggregation. However, we were not able to find any indication of aggregation in our samples. UV−vis−NIR before and after 4MBA addition did not show any indication of aggregation for all SERS samples. Reversible aggregation/association of NTs could be ruled out because of the presence of a sufficient amount of stabilizing agent (CTAB) in the solution. 4MBA is a commonly used Raman marker and not expected to induce particle aggregation. The single thiol and carboxyl groups of 4MBA would not be able to act as a molecular linker among particles. In addition, the amount of 4MBA added is much lower than that of the available CTAB (>50-fold molar excess). Also, the video feedback of the Raman microscopy did not give any indication of possible formation of aggregates even after the extended laser exposure. In the case of irreversible aggregation, we would expect a loss of particles over time, which was not observed. The AuNT dispersions were found to exhibit high colloidal stability for the reported surfactant concentrations, and the SERS responses could be detected reproducibly. Thus, we are confident that, even if aggregation (below the detection limit) would be present, it would be of negligible contribution and should not affect the registered SERS signals.

The SERS performance was quantified by a mean of the analytical enhancement factor (AEF), as defined by the ratio of the SERS intensity for the selected mode of a given analyte ($I_{\mathrm{SERS}}$) to the corresponding (nonenhanced) Raman intensity ($I_{\mathrm{RS}}$) under identical experimental conditions and at the respective concentrations, $c$, in the SERS and Raman experiments (see Section SI.5 and Figure S18).[67]

$$\mathrm{AEF} = \frac{I_{\mathrm{SERS}}/c_{\mathrm{SERS}}}{I_{\mathrm{RS}}/c_{\mathrm{RS}}} \qquad (1)$$

This definition is particularly well suited for SERS-active liquids (colloidal dispersions) and analytical chemistry applications, provided that all experimental procedures are clearly stated and a submonolayer coverage of the analyte is ensured.[67] The obtained AEFs range between (0.9−2.2) × $10^4$ at 1580 $\mathrm{cm}^{-1}$ and (1.6−5.6) × $10^4$ at 1070 $\mathrm{cm}^{-1}$ for a gold concentration of 250 $\mu$M (see Table S1) at 785 nm excitation. This result agrees well with the reported value of 1.2 × $10^5$ by Scarabelli et al. for a different analyte (benzenethiol) and obtained at a gold concentration twice than that used by us (495 $\mu$M).[30] For Raman markers at nonresonant conditions, this result represents a remarkable high signal yield per mole Au (AEF/$c_{\mathrm{Au}}$ of approximately 2.24 × $10^5$ $\mathrm{mM}^{-1}$), which is among the highest AEF/$c_{\mathrm{Au}}$ efficiency values presented in the literature for SERS-active colloidal dispersions.[30,67] The enhancement in dispersion even compares well to substrate enhancement factors (SSEFs) of densely packed NT monolayers on solid supports reported by Liebig et al. (2.76 × $10^4$, 4-nitrothiophenol)[47] and monolayer-over-mirror substrates reported by Lee et al. (1.6 × $10^4$, 2-naphthalenethiol).[68]

For comparison, we also determined the SERS performance for excitation at 633 nm and found the same trends as for the 785 nm laser. Maximum SERS intensity was found for AuNTs of $R = 5$ (see Figure S19). However, the overall signal yield was remarkably lower than that obtained at 785 nm. This could be explained by either losses by diffuse scattering contributions and the consequent limited laser penetration (into the dispersion) or differences in the SERS activity. Here, matching of the laser to the extinction maximum seems not to yield the best SERS activity. In fact, the extinction cross section and the confinement/enhancement of the electric nearfield are expected to exhibit a nonlinear scaling dependency. This off-resonant behavior has been reported earlier by Murphy et al. for nanorods.[69] The hotspot intensity is not directly correlated to the optical properties; thus, the extinction maximum is in many situations not the best excitation wavelength for SERS. An increase in SERS activity is generally expected for situations in which the laser line is shifted to the red, compared to the extinction maximum. Thus, the Stokes-shifted Raman signals would lie in the low-energy shoulder of the plasmon band. In our work, we found the highest SERS activity for the 785 nm laser line and for the particles of 100−130 nm size and extinction maxima between 630 and 670 nm, in line with the findings by Murphy et al.

The highest SERS enhancement could be identified at 785 nm excitation for the AuNT samples of $R = 5$ and 7.5 with AEFs of 4.9 × $10^4$ and 5.6 × $10^4$, respectively (Figure 6C, Table S1). Thus, these particles and laser wavelength were used for the quantification of the detection limit.

After that, to determine the limit of detection, aliquots of the AuNTs samples ($R = 5$ and 7.5) with a decreasing concentration of 4MBA (from $10^{-4}$ to $10^{-12}$ M) were prepared and tested. Figure 7 shows the SERS spectra of AuNTs ($R = 5$) at constant concentrations of Au (0.25 mM) and CTAB (0.5 mM) excited at 785 nm before (Figure 7A) and after background correction and spectral deconvolution by multipeak fitting (Figure 7B). In this study, we increased the CTAB concentration to increase the particle stability. In particular, the signals at 1070 ($\nu_{\mathrm{CC,ar.}}$, red), 1380 ($\nu_{\mathrm{CH,ali.}}$, green), and 1580

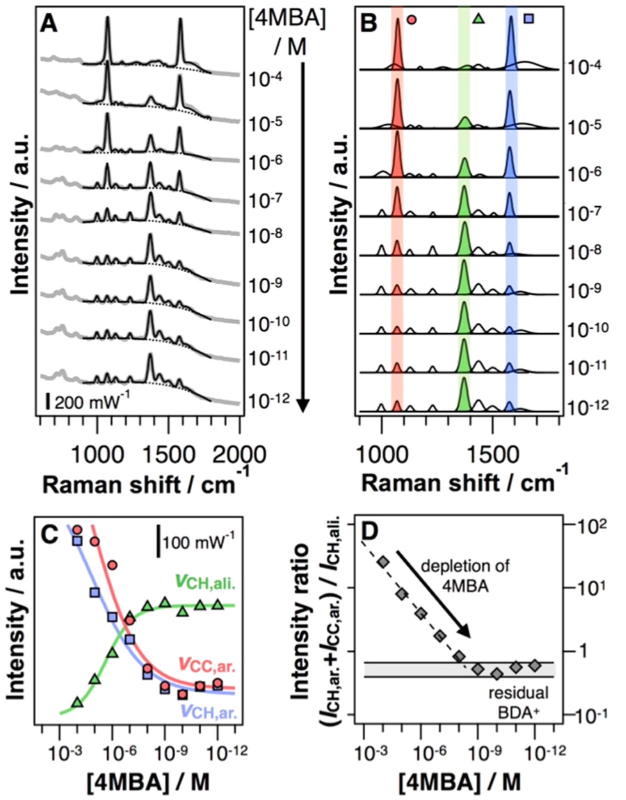

**Figure 7.** Limit of detection of 4MBA using CTAB-stabilized AuNTs ($R = 5$): (A) SERS spectra at constant concentrations of Au (0.25 mM) and CTAB (0.5 mM) excited at 785 nm (offset applied for clarity; before background correction). (B) Relative signal intensities and (C) concentration-dependent changes of the breathing mode ($\nu_{\mathrm{CC,ar.}}$, 1070 $\mathrm{cm}^{-1}$, red circles) and axial ring deformation ($\nu_{\mathrm{CH,ar.}}$, 1580 $\mathrm{cm}^{-1}$, blue squares) of the aromatic phenyl ring of 4MBA and skeletal vibrations ($\nu_{\mathrm{CH,ali.}}$, 1380 $\mathrm{cm}^{-1}$, green triangles) of the surfactant evaluated by multipeak fitting. (D) Linear decay of the intensity ratio of aromatic to aliphatic signals corresponding to a limit of detection of $10^{-8}$−$10^{-9}$ M. The plateau at lower concentrations (gray area) indicates a residual trace amount (1−10 nM) of the aromatic surfactant $\mathrm{BDA}^+$ at the AuNT interface, which originates from the particle synthesis using BDAC and could not be removed even after excessive washing with CTAB.

cm$^{-1}$ ($\nu_{CH,ar.}$, blue) exhibit distinct concentration-dependent changes in intensity. Because of its high binding affinity, 4MBA acts as a competing ligand to the stabilizing surfactant CTAB and can be considered to readily adsorb on the NT surface. Consequently, with decreasing 4MBA concentrations, the aromatic signals (CC and CH) are reduced because of their depletion on the AuNT surface (see Figure 7C). The coincident increase in the aliphatic signals ($\nu_{CH,ali.}$, green) can be attributed to the alkyl chain of the nonaromatic surfactant CTA$^+$ also present at the AuNT interface.[70] The linear decay of the intensity ratio of aromatic to aliphatic signals indicates a limit of detection of 4MBA of $10^{-8}$−$10^{-9}$ M (Figure 7D), which is in the same order of magnitude as for AuNTs obtained from a previously reported seed-mediated approach.[30] At lower 4MBA concentrations, a plateau value is reached, which indicates a residual amount of the aromatic surfactant BDA$^+$ originating from the particle synthesis performed using BDAC.[52] This trace amount of BDA$^+$ of 1−10 nM could not be removed even after excessive washing with CTAB. The data for AuNTs of $R$ = 7.5 agrees well with these findings (see Figure S20). Differences between binding affinities of nonaromatic (CTA$^+$) and aromatic (BDA$^+$) surfactants toward particle surfaces result from additional $\pi$-interactions of the electron-rich benzyl headgroup.[16] To the best of our knowledge, the nonquantitative nature of this ligand exchange has not been shown before. This proves that these particles provide high sensitivity for molecular sensing and quantitative information about the amount of molecules attached to the particle surface.

## CONCLUSIONS

We have presented a detailed study of the 3BA-mediated seedless synthesis of AuNTs and their use as large seeds for controlled Au overgrowth. First, we demonstrated that both temperature and solution pH need to be taken into account to obtain a high initial yield (50%) of monodisperse AuNT seeds of 30−55 nm size. Although the AuNT size can be controlled by its linear scaling with temperature from 70 to 95 °C, the AuNT shape yield depends critically on the solution pH. From pH 5.5 to 9.3, the synthesis gradually converts from thermodynamic to kinetic control with a consequent decease in the shape yield. Above pH 9.3, the anisotropic shape is completely lost, obtaining principally spherical morphologies. On the other hand, the concentration of the reducing agent (3BA) was found to not affect the shape yield of AuNTs.

Second, we investigated the seed-mediated overgrowth using the obtained AuNTs as seeds. Controlled by the molar ratio of $HAuCl_4$ to AuNT seeds ($R$), we prepared AuNTs between 100 and 180 nm in edge length and 50 and 80 nm in thickness while maintaining their triangular shape and tip sharpness. To the best of our knowledge, this is the first report in which well-defined gold triangles could be overgrown retaining their well-defined truncated triangular bipyramid morphology upon size increase. We employed TEM, FESEM, and SAXS to characterize the AuNT morphology, giving insight into the anisotropic nature of the seed-mediated overgrowth. The correlation of electron microscopy and SAXS analysis enabled us to quantify the ensemble-averaged tip sharpness, a key parameter for AuNT quality, and to follow its evolution upon an increase in size.

We determined the size-dependent SERS performance of the AuNTs using 4MBA as a model analyte yielding analytical enhancement factors (AEFs) between $0.9 \times 10^4$ and $5.6 \times 10^4$ for excitation at 785 nm. Maximum enhancement was identified for off-resonant excitation, that is, for AuNTs in the size range of 100−130 nm in edge length and 60−70 nm in thickness. The limit of detection was found to be between $10^{-9}$ and $10^{-10}$ M for a given particle concentration of 0.25 mM ([Au$^0$]). In addition, we found first evidence for the nonquantitative nature of the ligand exchange of aromatic (BDA$^+$) versus nonaromatic (CTA$^+$) surfactants. It was possible to detect a trace amount of BDA$^+$ of 1−10 nM, which originates from the AuNT seeds and could not be removed even after excessive washing with CTAB. This proves that these particles provide high sensitivity for SERS sensing and quantitative information about their molecular environment.

## ASSOCIATED CONTENT

### Supporting Information

The Supporting Information is available free of charge on the ACS Publications website at DOI: 10.1021/acsami.7b19081.

> Additional data for the particle synthesis; temperature-dependent and pH-dependent seed synthesis; TEM and FESEM image analysis; SAXS characterization and three-dimensional modeling; SERS analysis and data processing (PDF)

## AUTHOR INFORMATION

### Corresponding Authors

*E-mail: fery@ipfdd.de (A.F.).
*E-mail: rcontreras@uma.es (R.C.C.).

### ORCID

Christian Kuttner: 0000-0002-4093-7469
Stephan Förster: 0000-0002-7323-2449
Jorge Pérez-Juste: 0000-0002-4614-1699
Rafael Contreras-Cáceres: 0000-0001-6313-2340

### Present Address

$^\nabla$BioNanoPlasmonics Laboratory, CIC biomaGUNE, Paseo de Miramón 182, 20014 Donostia - San Sebastián, Spain (C.K.).

### Author Contributions

The manuscript was written through contributions of all authors. All authors have given approval for the final version of the manuscript.

### Notes

The authors declare no competing financial interest.

## ACKNOWLEDGMENTS

The research leading to these results has received funding from the Spanish MINECO grants CTQ2013-48418P, CTQ2016-76311-R, CTQ2017-84334R, and MAT2016-77809-R and from the Deutsche Forschungsgemeinschaft (DFG) within the Cluster of Excellence Centre for Advancing Electronics Dresden (cfaed). J.P.-J. also acknowledges financial support from Fundación Ramón Areces. C.K. acknowledges funding from the European Union's Horizon 2020 research and innovation programme under the Marie Skłodowska-Curie grant agreement No. 799393 (NANOBIOME).

## REFERENCES

(1) Park, S.-J.; Taton, T. A.; Mirkin, C. A. Array-Based Electrical Detection of DNA with Nanoparticle Probes. *Science* **2002**, *295*, 1503−1506.

(2) Storhoff, J. J.; Lucas, A. D.; Garimella, V.; Bao, Y. P.; Müller, U. R. Homogeneous Detection of Unamplified Genomic DNA Sequences

Based on Colorimetric Scatter of Gold Nanoparticle Probes. *Nat. Biotechnol.* **2004**, *22*, 883−887.

(3) Skrabalak, S. E.; Au, L.; Lu, X.; Li, X.; Xia, Y. Gold Nanocages for Cancer Detection and Treatment. *Nanomedicine* **2007**, *2*, 657−668.

(4) Sershen, S. R.; Westcott, S. L.; Halas, N. J.; West, J. L. Temperature-Sensitive Polymer-Nanoshell Composites for Photothermally Modulated Drug Delivery. *J. Biomed. Mater. Res.* **2000**, *51*, 293−298.

(5) El-Sayed, I. H.; Huang, X.; El-Sayed, M. A. Surface Plasmon Resonance Scattering and Absorption of Anti-EGFR Antibody Conjugated Gold Nanoparticles in Cancer Diagnostics: Applications in Oral Cancer. *Nano Lett.* **2005**, *5*, 829−834.

(6) Alvarez-Puebla, R. A.; Contreras-Cáceres, R.; Pastoriza-Santos, I.; Pérez-Juste, J.; Liz-Marzan, L. M. Au@pNIPAM Colloids as Molecular Traps for Surface-Enhanced, Spectroscopic, Ultra-Sensitive Analysis. *Angew. Chem., Int. Ed.* **2009**, *48*, 138−143.

(7) Tzounis, L.; Contreras-Cáceres, R.; Schellkopf, L.; Jehnichen, D.; Fischer, D.; Cai, C.; Uhlmann, P.; Stamm, M. Controlled Growth of Ag Nanoparticles Decorated Onto the Surface of SiO2 Spheres: a Nanohybrid System with Combined SERS and Catalytic Properties. *RSC Adv.* **2014**, *4*, 17846−17855.

(8) Hutter, E.; Fendler, J. H. Exploitation of Localized Surface Plasmon Resonance. *Adv. Mater.* **2004**, *16*, 1685−1706.

(9) Lee, K. S.; El-Sayed, M. A. Gold and Silver Nanoparticles in Sensing and Imaging: Sensitivity of Plasmon Response to Size, Shape, and Metal Composition. *J. Phys. Chem. B* **2006**, *110*, 19220−19225.

(10) He, Y. Q.; Liu, S. P.; Kong, L.; Liu, Z. F. A Study on the Sizes and Concentrations of Gold Nanoparticles by Spectra of Absorption, Resonance Rayleigh Scattering and Resonance Non-Linear Scattering. *Spectrochim. Acta, Part A* **2005**, *61*, 2861−2866.

(11) Yan, B.; Yang; Wang, Y. Comment on "Simulation of the Optical Absorption Spectra of Gold Nanorods as a Function of Their Aspect Ratio and the Effect of the Medium Dielectric Constant.". *J. Phys. Chem. B* **2003**, *107*, 9159.

(12) Pastoriza-Santos, I.; Liz-Marzan, L. M. Colloidal Silver Nanoplates. State of the Art and Future Challenges. *J. Mater. Chem.* **2008**, *18*, 1724−1737.

(13) Xue, C.; Métraux, G. S.; Millstone, J. E.; Mirkin, C. A. Mechanistic Study of Photomediated Triangular Silver Nanoprism Growth. *J. Am. Chem. Soc.* **2008**, *130*, 8337−8344.

(14) Schnepf, M. J.; Mayer, M.; Kuttner, C.; Tebbe, M.; Wolf, D.; Dulle, M.; Altantzis, T.; Formanek, P.; Förster, S.; Bals, S.; König, T. A. F.; Fery, A. Nanorattles with Tailored Electric Field Enhancement. *Nanoscale* **2017**, *9*, 9376−9385.

(15) Weissleder, R. A Clearer Vision for in Vivo Imaging. *Nat. Biotechnol.* **2001**, *19*, 316−317.

(16) Tebbe, M.; Kuttner, C.; Mayer, M.; Maennel, M.; Pazos-Perez, N.; König, T. A. F.; Fery, A. Silver-Overgrowth-Induced Changes in Intrinsic Optical Properties of Gold Nanorods: From Noninvasive Monitoring of Growth Kinetics to Tailoring Internal Mirror Charges. *J. Phys. Chem. C* **2015**, *119*, 9513−9523.

(17) Smith, A. M.; Mancini, M. C.; Nie, S. Second Window for in Vivo Imaging. *Nat. Nanotechnol.* **2009**, *4*, 710−711.

(18) Mayer, M.; Scarabelli, L.; March, K.; Altantzis, T.; Tebbe, M.; Kociak, M.; Bals, S.; Garcia de Abajo, F. J.; Fery, A.; Liz-Marzan, L. M. Controlled Living Nanowire Growth: Precise Control Over the Morphology and Optical Properties of AgAuAg Bimetallic Nanowires. *Nano Lett.* **2015**, *15*, 5427−5437.

(19) Hogan, N. J.; Urban, A. S.; Ayala-Orozco, C.; Pimpinelli, A.; Nordlander, P.; Halas, N. J. Nanoparticles Heat Through Light Localization. *Nano Lett.* **2014**, *14*, 4640−4645.

(20) Jain, P. K.; Lee, K. S.; El-Sayed, I. H.; El-Sayed, M. A. Calculated Absorption and Scattering Properties of Gold Nanoparticles of Different Size, Shape, and Composition: Applications in Biological Imaging and Biomedicine. *J. Phys. Chem. B* **2006**, *110*, 7238−7248.

(21) Tang, Z.; Kotov, N. A. One-Dimensional Assemblies of Nanoparticles: Preparation, Properties, and Promise. *Adv. Mater.* **2005**, *17*, 951−962.

(22) Guo, S.; Dong, S. Biomolecule-Nanoparticle Hybridsfor Electrochemical Biosensors. *TrAC, Trends Anal. Chem.* **2009**, *28*, 96−109.

(23) Li, C.; Shuford, K. L.; Chen, M.; Lee, E. J.; Cho, S. O. A Facile Polyol Route to Uniform Gold Octahedra with Tailorable Size and Their Optical Properties. *ACS Nano* **2008**, *2*, 1760−1769.

(24) Langille, M. R.; Personick, M. L.; Zhang, J.; Mirkin, C. A. Bottom-Up Synthesis of Gold Octahedra with Tailorable Hollow Features. *J. Am. Chem. Soc.* **2011**, *133*, 10414−10417.

(25) Pérez-Juste, J.; Liz-Marzán, L. M.; Carnie, S.; Chan, D. Y. C.; Mulvaney, P. Electric-Field-Directed Growth of Gold Nanorods in Aqueous Surfactant Solutions. *Adv. Funct. Mater.* **2004**, *14*, 571−579.

(26) Busbee, B. D.; Obare, S. O.; Murphy, C. J. An Improved Synthesis of High-Aspect-Ratio Gold Nanorods. *Adv. Mater.* **2003**, *15*, 414−416.

(27) Xue, C.; Mirkin, C. A. pH-Switchable Silver Nanoprism Growth Pathways. *Angew. Chem., Int. Ed.* **2007**, *46*, 2036−2038.

(28) Tao, A.; Sinsermsuksakul, P.; Yang, P. Polyhedral Silver Nanocrystals with Distinct Scattering Signatures. *Angew. Chem., Int. Ed.* **2006**, *45*, 4597−4601.

(29) Wiley, B.; Herricks, T.; Sun, Y.; Xia, Y. Polyol Synthesis of Silver Nanoparticles: Use of Chloride and Oxygen to Promote the Formation of Single-Crystal, Truncated Cubes and Tetrahedrons. *Nano Lett.* **2004**, *4*, 1733−1739.

(30) Scarabelli, L.; Coronado-Puchau, M.; Giner-Casares, J. J.; Langer, J.; Liz-Marzán, L. M. Monodisperse Gold Nanotriangles: Size Control, Large-Scale Self-Assembly, and Performance in Surface-Enhanced Raman Scattering. *ACS Nano* **2014**, *8*, 5833−5842.

(31) Chen, L.; Ji, F.; Xu, Y.; He, L.; Mi, Y.; Bao, F.; Sun, B.; Zhang, X.; Zhang, Q. High-Yield Seedless Synthesis of Triangular Gold Nanoplates Through Oxidative Etching. *Nano Lett.* **2014**, *14*, 7201−7206.

(32) Li, C.; Li, D.; Wan, G.; Xu, J.; Hou, W. Facile Synthesis of Concentrated Gold Nanoparticles with Low Size-Distribution in Water: Temperature and pH Controls. *Nanoscale Res. Lett.* **2011**, *6*, No. 440.

(33) Briñas, R. P.; Hu, M.; Qian, L.; Lymar, E. S.; Hainfeld, J. F. Gold Nanoparticle Size Controlled by Polymeric Au(I) Thiolate Precursor Size. *J. Am. Chem. Soc.* **2008**, *130*, 975−982.

(34) Wang, S.; Qian, K.; Bi, X.; Huang, W. Influence of Speciation of Aqueous HAuCl 4on the Synthesis, Structure, and Property of Au Colloids. *J. Phys. Chem. C* **2009**, *113*, 6505−6510.

(35) Rodríguez-Fernández, J.; Pérez-Juste, J.; Garcia de Abajo, F. J.; Liz-Marzan, L. M. Seeded Growth of Submicron Au Colloids with Quadrupole Plasmon Resonance Modes. *Langmuir* **2006**, *22*, 7007−7010.

(36) Jana, N. R.; Gearheart, L.; Murphy, C. J. Evidence for Seed-Mediated Nucleation in the Chemical Reduction of Gold Salts to Gold Nanoparticles. *Chem. Mater.* **2001**, *13*, 2313−2322.

(37) Zsigmondy, R.; Norton, J. F.; Spear, E. B. *The Chemistry of Colloids*; John Wiley & Sons, Inc., New York, 1917.

(38) Sánchez-Iglesias, A.; Winckelmans, N.; Altantzis, T.; Bals, S.; Grzelczak, M.; Liz-Marzan, L. M. High-Yield Seeded Growth of Monodisperse Pentatwinned Gold Nanoparticles Through Thermally Induced Seed Twinning. *J. Am. Chem. Soc.* **2017**, *139*, 107−110.

(39) Lofton, C.; Sigmund, W. Mechanisms Controlling Crystal Habits of Gold and Silver Colloids. *Adv. Funct. Mater.* **2005**, *15*, 1197−1208.

(40) Millstone, J. E.; Hurst, S. J.; Métraux, G. S.; Cutler, J. I.; Mirkin, C. A. Colloidal Gold and Silver Triangular Nanoprisms. *Small* **2009**, *5*, 646−664.

(41) Zeng, J.; Xia, X.; Rycenga, M.; Henneghan, P.; Li, Q.; Xia, Y. Successive Deposition of Silver on Silver Nanoplates: Lateral Versus Vertical Growth. *Angew. Chem., Int. Ed.* **2011**, *50*, 244−249.

(42) Millstone, J. E.; Métraux, G. S.; Mirkin, C. A. Controlling the Edge Length of Gold Nanoprisms via a Seed-Mediated Approach. *Adv. Funct. Mater.* **2006**, *16*, 1209−1214.

DOI: 10.1021/acsami.7b19081
*ACS Appl. Mater. Interfaces* 2018, 10, 11152−11163

(43) Walker, D. A.; Browne, K. P.; Kowalczyk, B.; Grzybowski, B. A. Self-Assembly of Nanotriangle Superlattices Facilitated by Repulsive Electrostatic Interactions. *Angew. Chem., Int. Ed.* **2010**, *49*, 6760−6763.

(44) Young, K. L.; Jones, M. R.; Zhang, J.; Macfarlane, R. J.; Esquivel-Sirvent, R.; Nap, R. J.; Wu, J.; Schatz, G. C.; Lee, B.; Mirkin, C. A. Assembly of Reconfigurable One-Dimensional Colloidal Superlattices Due to a Synergy of Fundamental Nanoscale Forces. *Proc. Natl. Acad. Sci. U.S.A.* **2012**, *109*, 2240−2245.

(45) Liebig, F.; Sarhan, R. M.; Prietzel, C.; Reinecke, A.; Koetz, J. "Green" Gold Nanotriangles: Synthesis, Purification by Polyelectrolyte/Micelle Depletion Flocculation and Performance in Surface-Enhanced Raman Scattering. *RSC Adv.* **2016**, *6*, 33561−33568.

(46) Liebig, F.; Thünemann, A. F.; Koetz, J. Ostwald Ripening Growth Mechanism of Gold Nanotriangles in Vesicular Template Phases. *Langmuir* **2016**, *32*, 10928−10935.

(47) Liebig, F.; Sarhan, R. M.; Sander, M.; Koopman, W.; Schuetz, R.; Bargheer, M.; Koetz, J. Deposition of Gold Nanotriangles in Large Scale Close-Packed Monolayers for X-Ray-Based Temperature Calibration and SERS Monitoring of Plasmon-Driven Catalytic Reactions. *ACS Appl. Mater. Interfaces* **2017**, *9*, 20247−20253.

(48) Straney, P. J.; Diemler, N. A.; Smith, A. M.; Eddinger, Z. E.; Gilliam, M. S.; Millstone, J. E. Ligand-Mediated Deposition of Noble Metals at Nanoparticle Plasmonic Hotspots. *Langmuir* **2018**, *34*, 1084−1091.

(49) Langille, M. R.; Personick, M. L.; Zhang, J.; Mirkin, C. A. Defining Rules for the Shape Evolution of Gold Nanoparticles. *J. Am. Chem. Soc.* **2012**, *134*, 14542−14554.

(50) González-Rubio, G.; de Oliveira, T. M.; Altantzis, T.; La Porta, A.; Guerrero-Martínez, A.; Bals, S.; Scarabelli, L.; Liz-Marzan, L. M. Disentangling the Effect of Seed Size and Crystal Habit on Gold Nanoparticle Seeded Growth. *Chem. Commun.* **2017**, *53*, 11360−11363.

(51) Gole, A.; Murphy, C. J. Seed-Mediated Synthesis of Gold Nanorods: Role of the Size and Nature of the Seed. *Chem. Mater.* **2004**, *16*, 3633−3640.

(52) Casado-Rodriguez, M. A.; Sanchez-Molina, M.; Lucena-Serrano, A.; Lucena-Serrano, C.; Rodriguez-Gonzalez, B.; Algarra, M.; Diaz, A.; Valpuesta, M.; Lopez-Romero, J. M.; Pérez-Juste, J.; Contreras-Caceres, R. Synthesis of Vinyl-Terminated Au Nanoprisms and Nanooctahedra Mediated by 3-Butenoic Acid: Direct Au@pNIPAM Fabrication with Improved SERS Capabilities. *Nanoscale* **2016**, *8*, 4557−4564.

(53) Gómez-Graña, S.; Fernández-López, C.; Polavarapu, L.; Salmon, J.-B.; Leng, J.; Pastoriza-Santos, I.; Pérez-Juste, J. Gold Nanooctahedra with Tunable Size and Microfluidic-Induced 3D Assembly for Highly Uniform SERS-Active Supercrystals. *Chem. Mater.* **2015**, *27*, 8310−8317.

(54) Wickens, Z. K.; Skakuj, K.; Morandi, B.; Grubbs, R. H. Catalyst-Controlled Wacker-Type Oxidation: Facile Access to Functionalized Aldehydes. *J. Am. Chem. Soc.* **2014**, *136*, 890−893.

(55) Smith, K. W.; Yang, J.; Hernandez, T.; Swearer, D. F.; Scarabelli, L.; Zhang, H.; Zhao, H.; Moringo, N. A.; Chang, W.-S.; Liz-Marzan, L. M.; Ringe, E.; Nordlander, P.; Link, S. Environmental Symmetry Breaking Promotes Plasmon Mode Splitting in Gold Nanotriangles *J. Phys. Chem. C* 2017, 10.1021/acs.jpcc.7b08428.

(56) Park, K.; Koerner, H.; Vaia, R. A. Depletion-Induced Shape and Size Selection of Gold Nanoparticles. *Nano Lett.* **2010**, *10*, 1433−1439.

(57) Bastús, N. G.; Comenge, J.; Puntes, V. Kinetically Controlled Seeded Growth Synthesis of Citrate-Stabilized Gold Nanoparticles of Up to 200 Nm: Size Focusing Versus Ostwald Ripening. *Langmuir* **2011**, *27*, 11098−11105.

(58) Rodríguez-Fernández, J.; Pérez-Juste, J.; Mulvaney, P.; Liz-Marzan, L. M. Spatially-Directed Oxidation of Gold Nanoparticles by Au(III)-CTAB Complexes. *J. Phys. Chem. B* **2005**, *109*, 14257−14261.

(59) Shuford, K. L.; Ratner, M. A.; Schatz, G. C. Multipolar Excitation in Triangular Nanoprisms. *J. Chem. Phys.* **2005**, *123*, No. 114713.

(60) Kim, J.; Song, X.; Ji, F.; Luo, B.; Ice, N. F.; Liu, Q.; Zhang, Q.; Chen, Q. Polymorphic Assembly From Beveled Gold Triangular Nanoprisms. *Nano Lett.* **2017**, *17*, 3270−3275.

(61) Luo, B.; Smith, J. W.; Wu, Z.; Kim, J.; Ou, Z.; Chen, Q. Polymerization-Like Co-Assembly of Silver Nanoplates and Patchy Spheres. *ACS Nano* **2017**, *11*, 7626−7633.

(62) Höller, R. P. M.; Dulle, M.; Thomä, S.; Mayer, M.; Steiner, A. M.; Förster, S.; Fery, A.; Kuttner, C.; Chanana, M. Protein-Assisted Assembly of Modular 3D Plasmonic Raspberry-Like Core/Satellite Nanoclusters: Correlation of Structure and Optical Properties. *ACS Nano* **2016**, *10*, 5740−5750.

(63) Huergo, M. A.; Maier, C. M.; Castez, M. F.; Vericat, C.; Nedev, S.; Salvarezza, R. C.; Urban, A. S.; Feldmann, J. Optical Nanoparticle Sorting Elucidates Synthesis of Plasmonic Nanotriangles. *ACS Nano* **2016**, *10*, 3614−3621.

(64) Mir-Simon, B.; Reche-Perez, I.; Guerrini, L.; Pazos-Perez, N.; Alvarez-Puebla, R. A. Universal One-Pot and Scalable Synthesis of SERS Encoded Nanoparticles. *Chem. Mater.* **2015**, *27*, 950−958.

(65) Bishnoi, S. W.; Rozell, C. J.; Levin, C. S.; Gheith, M. K.; Johnson, B. R.; Johnson, D. H.; Halas, N. J. All-Optical Nanoscale pH Meter. *Nano Lett.* **2006**, *6*, 1687−1692.

(66) Burikov, S.; Dolenko, T.; Patsaeva, S.; Starokurov, Y.; Yuzhakov, V. Raman and IR Spectroscopy Research on Hydrogen Bonding in Water-Ethanol Systems. *Mol. Phys.* **2010**, *108*, 2427−2436.

(67) Le Ru, E. C.; Blackie, E.; Meyer, M.; Etchegoin, P. G. Surface Enhanced Raman Scattering Enhancement Factors: a Comprehensive Study. *J. Phys. Chem. C* **2007**, *111*, 13794−13803.

(68) Lee, Y. H.; Lee, C. K.; Tan, B.; Rui Tan, J. M.; Phang, I. Y.; Ling, X. Y. Using the Langmuir-Schaefer Technique to Fabricate Large-Area Dense SERS-Active Au Nanoprism Monolayer Films. *Nanoscale* **2013**, *5*, 6404−6412.

(69) Sivapalan, S. T.; Devetter, B. M.; Yang, T. K.; van Dijk, T.; Schulmerich, M. V.; Carney, P. S.; Bhargava, R.; Murphy, C. J. Off-Resonance Surface-Enhanced Raman Spectroscopy From Gold Nanorod Suspensions as a Function of Aspect Ratio: Not What We Thought. *ACS Nano* **2013**, *7*, 2099−2105.

(70) Tebbe, M.; Kuttner, C.; Männel, M.; Fery, A.; Chanana, M. Colloidally Stable and Surfactant-Free Protein-Coated Gold Nanorods in Biological Media. *ACS Appl. Mater. Interfaces* **2015**, *7*, 5984−5991.

## ■ NOTE ADDED AFTER ASAP PUBLICATION

This paper was published on the Web on March 20, 2018. Additional text corrections were implemented throughout the paper, and the paper was reposted on March 21, 2018.